Dyes and Pigments 219 (2023) 111561

Contents lists available at ScienceDirect

Dyes and Pigments

journal homepage: www.elsevier.com/locate/dyepig

BODIPY doping of covalent organic frameworks-based nanomaterials: A novel strategy towards biomedical applications

Fátima Suárez-Blas [a,b,1], Marcos Martínez-Fernández [a,1], Alejandro Prieto-Castañeda [a], Alba García-Fernández [c,d,e], José I. Martínez [f], María Mar Ramos [b], María J. Ortiz [a,**], Ramón Martínez-Máñez [c,d,e,g,***], José L. Segura [a,*]

[a] Departamento de Química Orgánica, Facultad de CC. Químicas, Universidad Complutense de Madrid, 28040, Madrid, Spain
[b] Departamento de Tecnología Química y Medioambiental, Universidad Rey Juan Carlos, 28933, Móstoles, Spain
[c] Instituto Interuniversitario de Investigación de Reconocimiento Molecular y Desarrollo Tecnológico (IDM), Universitat Politècnica de València, Universitat de València, 46022, Valencia, Spain
[d] Unidad Mixta UPV-CIPF de Investigación en Mecanismos de Enfermedades y Nanomedicina, Centro de Investigación Príncipe Felipe, Universitat Politècnica de València, 46012, Valencia, Spain
[e] CIBER de Bioingeniería, Biomateriales y Nanomedicina, Instituto de Salud Carlos III, Spain
[f] Departamento de Nanoestructuras, Superficies, Recubrimientos y Astrofísica Molecular, Instituto de Ciencia de Materiales de Madrid (ICMM-CSIC), 28049, Madrid, Spain
[g] Unidad Mixta de Investigación en Nanomedicina y Sensores, IIS La Fe, Universitat Politècnica de València, 46026, Valencia, Spain

ARTICLE INFO

Keywords:
COF
BODIPY
Internalization
Doping
Frameworks

ABSTRACT

Covalent organic Frameworks (COFs) are a class of crystalline macromolecular materials build-up by monomers with specific symmetries or functionalities. There are important limitations in the synthesis of highly ordered COFs, such as the shape and packing of the building blocks. Thus, the presence of fluorine atoms that lie perpendicular to the bisecting plane of BODIPY derivatives together with the presence of four bulky methyl groups could hinder the crystallization process in COF synthesis. For that reason, BODIPY-based COFs are rarely incorporated to COF networks. In this work, following the mixed linker strategy, a pre-synthetic method to dope COF structures with BODIPY units was developed. The materials have been processed into fluorescent Covalent Organic Nanosheets (CONs) with defined particle-size distributions around 100 nm, suitable for cellular biomedical applications. The viability of the CONs was evaluated using Sk-Mel-103 cells, demonstrating the internalization showing 100% cell viability. We envisage that this work could accelerate the discovery of new COF-based materials for biomedical sciences.

1. Introduction

Two-dimensional covalent organic frameworks (COFs) are a part of the full mosaic which comprises crystalline and porous materials. Since the prominent work of O. M. Yaghi and co-workers in 2005 [1] the interest in these materials have increased exponentially [2]. COFs are built up through the formation of dynamic covalent bonds to ensure the crystallization processes by the curing of the networks through equilibrium reactions [2–4]. With this aim, the formation of several reversible bonds were investigated including imine [4], imide [5], triazine [6] or vinylene [7] linkages. The properties of the networks are a function of the monomers or linkers which build up the structure [8,9]. However, to achieve the crystalline phase, the use of crystallization processes requires usually planar monomers functionalized in specific positions, limiting the structural variability [8,10]. Some strategies have been developed to increase the number of units accessible to yield crystalline and porous materials *via* post-synthetic or pre-synthetic procedures [11]. Some of them are pendant group reactions [12,13]

* Corresponding author.
** Corresponding author.
*** Corresponding author. Instituto Interuniversitario de Investigación de Reconocimiento Molecular y Desarrollo Tecnológico (IDM), Universitat Politècnica de València, Universitat de València, 46022, Valencia, Spain.
E-mail addresses: mjortiz@quim.ucm.es (M.J. Ortiz), rmaez@qim.upv.es (R. Martínez-Máñez), segura@ucm.es (J.L. Segura).
[1] Fátima Suárez-Blas and Marcos Martínez-Fernández contributed equally to this work.

https://doi.org/10.1016/j.dyepig.2023.111561
Received 20 April 2023; Received in revised form 22 June 2023; Accepted 21 July 2023
Available online 24 July 2023

or pore wall modifications [14–16] which usually reduce the crystalline or porous features. For this reason, an emerging strategy is to incorporate the desired building blocks as a "dopant" in the COF network [17]. This approach is similar to the mixed linker strategy reported before which comprises several protocols such as monomer truncation, hetero/homo-structural mixed linkers, linker feed variation or monomer ratio [2,18,19], with the difference of the low amounts employed of one of the linkers. Skeleton doping consists in a three-component reaction in which at least two molecules have similar structural properties such as relative angles and distance between the reactive points. In this manner, the incorporation of linkers, which by themselves would arise poor crystalline structures, could be incorporated into pre-synthetic periodic networks thus inhibiting the decrease on the crystalline and porosity features.

Boron dipyrromethenes (BODIPYs or 4,4-difluoro-4-bora-3a,4a-diaza-*s*-indacenes) are a small but extremely versatile class of fluorescent dyes, which were accidently discovered in 1968 by Treibs and Kreuzer [20,21]. They were re-discovered after 20 years of forgetfulness and deeply studied in the early 1990s, [22,23] achieving exponential growth in their development until nowadays [24,25]. Some of the outstanding photophysical features of BODIPY dyes include their high quantum efficiencies of fluorescence, high molar extinction coefficients, and easy electronic modification of frontier molecular orbitals by substituents. Thus, because of their easily tuneable properties, a wide range of versatile and important applications have been found for BODIPY dyes in different fields of research, including optoelectronic materials [26], OLEDs [24], solar cells [27], laser dyes [28], sensors [29], photodynamic therapy [30–34], bioimaging [35] and other emerging applications such as the development of theragnostic agents [30,36–39] or systems with absorption/emission in the NIR and NIR II [40–42] within the therapeutic window.

In this regard, COFs can be considered as one of the most powerful nanoscale platforms for the integration of organic fluorophores and photosensitizers due to their superb characteristics such as their intrinsic porosity, their enhanced chemical stability and their easy-to-functionalize nature compared to other organic nanomaterials [43–48]. However, the production of BODIPY@COF hybrids is still not widely studied, and the few approaches reported so far only involves "decoration" of the COF by means of post-synthetic end group functional reactions, as depicted in Scheme 1 [49–53]. The use of this post-synthetic approach furnishes a heterogeneous distribution of dopants, only recovering the external structure of the COF particles (Scheme 1, bottom) [51,53]. This could enhance long-time stability of these nanomaterials by avoiding core-shell distributions obtained by decoration. However, despite the benefits expected for the inclusion of BODIPY dyes as structural unit of a COF backbone, the presence of the characteristic sp^3 centres in BODIPY derivatives produce steric interactions that prevent the formation of porous and crystalline COFs formed only with BODIPY-based monomers.

In this article, we want to explore a strategy that allows the incorporation of BODIPY dye-based monomers as part of the skeleton of a crystalline COF but simultaneously avoids the excessive steric interactions that would be associated to the polymerization and crystallization only with BODIPY dye-based monomers. With this aim, we have synthesized a suitably functionalized BODIPY dye (2,6-diformyl-1,3,5,7-tetramethyl-BODIPY, **BDPDA**, Scheme 2) with the right length and shape to integrate it in a crystalline COF endowed with the isostructural 4,4′-biphenyldialdehyde (**BPDA**) [19] as shown in Scheme 2. As a co-monomer we have chosen the tetratopic 4,4′,4″,4‴-(ethene-1,1,2,2-tetrayl)tetraaniline (**ETTA**) due to: (i) the production of a dual-pore Kagome network, which could be interesting to enhance the ROS diffusion through the COF pores or to encapsulate drugs with different sizes for combined therapy in future applications [49], and (ii) the efficient packing modes of the ETTA monomer, which are known to favour the crystallization processes [54]. In Scheme 2 is depicted the co-crystallization between **BPDA** and **ETTA**, with controlled amounts of **BDPDA** to produce COFs doped with the BODIPY units homogeneously integrated in the COF skeleton (**BDP$_{X\%}$-COF**). By using this strategy, we avoid the loss of the porous and crystalline features of the COF while

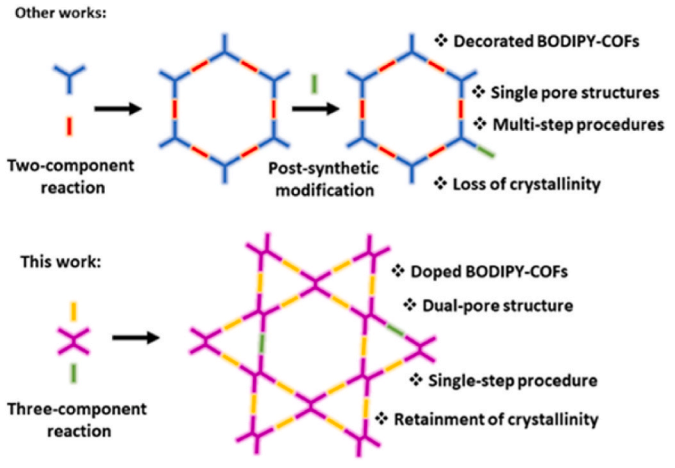

Scheme 1. Cartoon representation for the synthesis of BODIPY-based COFs: **(top)** the two-step synthetic approach used so far. **(bottom)** the single-step synthetic approach followed in this work. BODIPY-based building blocks are represented as green pieces.

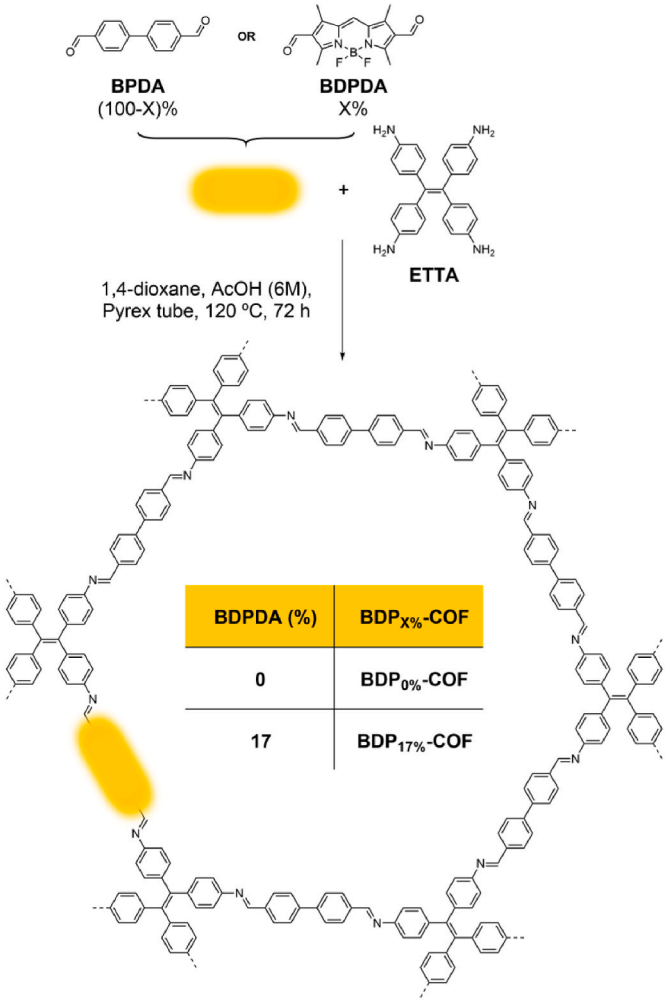

Scheme 2. BDPX%-COF synthesis (the "x" represents the percentage of BDP loaded as depicted on inset table).

adding the optical properties of the fluorophore.

Due to the excellent chemical and structural stability of the novel COF, we will address also its processability *via* liquid phase exfoliation [55,56] by disrupting the interlayer interactions of the network to obtain dispersible fluorescent covalent organic nanosheets (CONs) with sizes around 100 nm in water. Finally, given the interest in extending the applicability of COF-based nanomaterials in the biomedical field, we evaluate the toxic effect and the internalization of the CONs in Sk-Mel-103 cancer cells.

2. Experimental section

2.1. General methods

ETTA was synthetized according to a previously reported protocol [17]. Common solvents were dried and distilled by standard procedures. Flash chromatography was performed using silica gel 60 (230–400 mesh). NMR spectra were recorded using $CDCl_3$ at 20 °C on a Bruker Avance DPX-300 (300 MHz for ^{1}H and 75 MHz for ^{13}C) and a Bruker Avance III (700 MHz for ^{1}H and 176 MHz for ^{13}C). ^{1}H NMR and ^{13}C NMR chemical shifts (δ) were referenced to internal solvent $CDCl_3$ ($\delta = 7.260$ and 77.16 ppm, respectively). DEPT 135 experiments were used to determine the type of carbon nucleus (C *vs* CH *vs* CH_2 *vs* CH_3). High resolution mass spectrometry (HRMS) was performed using the MALDI-TOF technique. FTIR was performed on a Bruker TENSOR 27 on a diamond plate (ATR). PXRD was carried out on a X'PERT MPD with conventional Bragg-Brentano geometry using monochromatic Cu Kα1 radiation (λ = 1.5406 Å) in the $2\theta = 2°–40°$ range. Solid state ^{13}C CP/MAS NMR spectra were recorded on a Bruker AVANCE III HD-WB 400 MHz employing rotation frequency of 12 kHz. Nitrogen sorption isotherms. N_2 (77 K) adsorption-desorption was performed with a Micromeritics Tristar 3000 and the COFs were previously activated for 4 h at $<10^{-7}$ bar and 120 °C. TGA was analysed with a TGA-Q50 instrument using a platinum plate with a heating rate of 10 °C/min. Solution. TEM micrographs were recorded in a JEOL JEM 1400 TEM at 200 kV and SEM was recorded in a JEOL JSM7600F. Ultraviolet–Visible (UV–vis) spectrums were recorded in a Varian Cary 50 scan spectrometer and emission spectra was recorded in a JASCO FP-6300.

2.1.1. Cell culture

The human melanoma cell line SK-Mel-103 was cultured in Dulbecco's Modified Eagle Medium (DMEM) supplemented with 10% fetal bovine serum (FBS) and maintained at 37 °C in an atmosphere of 20% O_2 and 5% CO_2.

2.1.2. Cell Viability Assays

Sk-Mel-103 cells were seeded in 96-well plates at 5000 cells/well and incubated for 24 h. Then, cells were treated with different concentrations of **$BDP_{0\%}$-COF** and **$BDP_{17\%}$-COF**, ranging from 0 to 250 μg/mL (DMEM) for 48 h. Then, cell viability was measured by using the WST-1 Assay for Cell Proliferation and Viability (Roche). For that purpose, 7 μL of WST-1 were added to each well and the plates were incubated for 1 h at 37 °C. The absorbance of samples was measured using a spectrophotometer Wallac 1420 Victor2 Microplate Reader (PerkinElmer) at a wavelength of 450 nm.

2.1.3. Cell uptake Assays

Sk-Mel-103 cells were seed on glass coverslips in 6-well plates and incubated for 24 h. Then, cells were incubated with the **$BDP_{17\%}$-COF** for 4, 24, 48 and 72 h in the presence of cell membrane maker (5 μg/mL, Wheat Germ Agglutinin Alexa Fluor™ 647 Conjugate, Invitrogen Ref. W32466). Slides were washed, DNA marker (2 μg/mL, Hoechst 33342) added, and slides were visualized under a confocal microscope Leica TCS SP8 HyVolution II.

2.2. Synthesis of BODIPYs

2.2.1. General procedure for formylation reactions of BODIPYs

2-formyl-1,3,5,7-tetramethyl-BODIPY (**BDPMA**) was synthesized by the corresponding described method [57,58]. A mixture of $POCl_3$ (15–30 equiv) and DMF (30–60 equiv) was stirred in an ice bath for 5 min under argon. After being warmed to rt, it was stirred for additional 30 min, and then, BODIPY (1 equiv) in DCE or DCM was added. The reaction was raised to 60 °C or reflux and stirred for 1–48 h. The reaction progress was monitored by TLC. Once the reaction was completed, the mixture was cooled to rt and slowly poured into saturated aqueous $NaHCO_3$ (100 mL) under ice-cold conditions, and stirring maintained for 1 h. Finally, the reaction mixture was diluted with DCM and washed with H_2O. The organic layer was dried over anhydrous Na_2SO_4, filtered and evaporated to dryness. The obtained residue was submitted to purification by flash chromatography on silica gel.

2.2.2. 2-formyl-1,3,5,7-tetramethyl-BODIPY (BDPMA)

According to general procedure for the formylation reactions, $POCl_3$ (1.13 mL, 12.1 mmol), DMF (1.87 mL, 24.2 mmol) and 1,3,5,7-tetramethyl-BODIPY (PM505/515, 200 mg, 0.80 mmol) in DCE (40 mL) were reacted at 60 °C for 1 h. Flash chromatography using hexane/DCM (40:60) afforded **BDPMA** [57] (218.7 mg, 99%) as an orange solid. **^{1}H NMR (300 MHz, $CDCl_3$)** δ 10.04 (s, 1H, CHO), 7.23 (s, 1H, CH), 6.22 (s, 1H, CH), 2.78 (s, 3H, CH_3), 2.60 (s, 3H, CH_3), 2.52 (s, 3H, CH_3), 2.31 (s, 3H, CH_3) ppm.

2.2.3. 2,6-diformyl-1,3,5,7-tetramethyl-BODIPY (BDPDA)

According to general procedure for the formylation reactions, $POCl_3$ (2.0 mL, 21.6 mmol), DMF (3.33 mL, 43.2 mmol) and **BDPMA** (200 mg, 0.72 mmol) in DCM (40 mL) were reacted at reflux for 48 h. Flash chromatography using hexane/DCM/EtOAc (40:50:10) afforded **BDPDA** (179.5 mg, 82%) as a red solid. **^{1}H NMR (700 MHz, $CDCl_3$)** δ 10.11 (s, 2H, 2CHO), 7.51 (s, 1H, CH), 2.86 (s, 6H, $2CH_3$), 2.61 (s, 6H, $2CH_3$) ppm. **^{13}C NMR (176 MHz, $CDCl_3$)** δ 185.4 (CHO), 162.1 (C), 146.5 (C), 133.7 (C), 127.6 (C), 124.7 (CH), 13.9 (CH_3), 10.7 (CH_3) ppm. **FTIR (ATR)** ν 2921, 2849, 1665, 1600, 1467, 1402, 1370, 1342, 1247, 1141, 1093, 1009, 934, 896, 781 cm^{-1}. **HRMS-MALDI-TOF** *m/z* calcd. for $C_{15}H_{15}BF_2N_2O_2$: 304.1195; found: 304.1190.

2.3. Synthesis and characterization of COFs

2.3.1. General procedure for COF synthesis

To a Pyrex Vessel (internal diameter: 18 mm, height: 11 cm) were introduced ETTA, BPDA and BDPDA using the quantities specified for each case. Then, 1,4-dioxane was added, dragging the contents from the vessel walls. The vessel was subjected to an ultrasonic bath (35 kHz, 80 W) for 5 min to homogenize the suspension. Then, AcOH (6 M, 0.06 mL) was added, observing the polymerization of the system. The vessel was degassed by three freeze-thaw cycles using liquid nitrogen and argon. Finally, the vessel was flame-sealed under vacuum and heated at 120 °C for 3 days in a graphite bath. After this time, the precipitate was filtered by gravity and washed using the solvents specified for each case. Finally, the solid was dried in air and under vacuum at 100 °C, obtaining the desired COFs.

2.3.2. $BDP_{0\%}$-COF

According to general procedure for the COF synthesis, ETTA (18.69 mg, 0.047 mmol) and BPDA (20 mg, 0.09 mmol) were dissolved in 1,4-dioxane (0.62 mL). Then, AcOH (0.062 mL) was added, and the mixture was allowed to react. The precipitate was filtered and washed with THF, EtOH, acetone (6 times for 36 h) and hexane (3 times for 24 h) air-dried and vacuum dried. After drying, $BDP_{0\%}$-COF (30.5 mg, 87%) was obtained as a yellow powder. ^{13}C NMR (100 MHz, ss-CP/MAS) δ 159.25, 151.65, 143.22, 137.26, 131.07, 127.86, 121.15 ppm. FTIR (ATR) ν 1700, 1619, 1601, 1515, 1497, 1310, 1284, 1196, 1164, 1105, 1003,

970, 883, 835, 815, 786, 734, 648 cm^{-1}. PXRD 2θ (°) 2.20°, 3.94°, 4.44°, 6.67°, 7.95° 8.84°.

2.3.3. $BDP_{17\%}$-COF

According to general procedure for the COF synthesis, ETTA (18.69 mg, 0.047 mmol), BPDA (16.62 mg, 0.079 mmol) and BDPDA (49.2 mg, 0.016 mmol) were dissolved in 1,4-dioxane (0.62 mL). Then, AcOH (6 M, 0.062 mL) was added, and the mixture was allowed to react. The precipitate was filtered and washed with THF, EtOH, $CHCl_3$, acetone (until the residues no longer fluoresce) and hexane (3 times for 24 h), air-dried and vacuum dried. After drying, $BDP_{17\%}$-COF (31 mg, 84%) was obtained as a greenish black powder. ^{13}C NMR (100 MHz, ss-CP/MAS) δ 159.59, 150.19, 143.48, 137.52, 130.88, 128.42, 121.93, 12.08 ppm. FTIR (ATR) ν 1700, 1619, 1603, 1575, 1497, 1310, 1235, 1191, 1169, 1105, 1003, 973, 885, 835, 815, 743, 722, 651 cm^{-1}. PXRD 2θ (°) 2.20°, 3.81°, 4.48°, 6.61°, 7.96°, 8.79°.

2.4. Theoretical methods, computational details and structural modelling

2.4.1. Molecular fragments

As starting point for the theoretical analysis, molecular units participating in the formation of the **$BDP_{0/17\%}$-COF** systems were computed in their gas-phase by using Density Functional Theory (DFT) as implemented in the Gaussian16 simulation package [59] by adopting the hybrid functional CAM-B3LYP [60] to account for the electronic exchange-correlation (XC) effects and the cc-pVDZ basis set [61] to model the different atomic species. Along the relaxation processes, all geometrical parameters were allowed to vary independently, and the calculated geometries were confirmed as energy minima by frequency calculations. The optimized geometries of the molecular "building blocks" will be used in the construction of suitable starting-point periodic COF models. Gaussian16 simulation package was also employed to compute the UV–Vis photoabsorption spectra of the most representative molecular fragments of the **$BDP_{x\%}$-COF** compounds, which were calculated by using Time-dependent Density Functional Theory (TDDFT) [62]. For the computation of the optical excitations, and in order to closely mimic the experimental conditions, we have included the effect of the experimentally used solvent within the Polarizable Continuum Model (PCM) [63] by considering an effective dielectric constant of $\varepsilon = 30$ (corresponding to a 7:3 THF/H_2O solution), which has resulted to provide excellent results in previous literature by our group [12].

2.4.2. Periodic systems

On the basis of the pre-optimized molecular "building blocks" obtained, we used periodic boundary conditions to perform geometry optimization of a battery of stacked 3D layered **$BDP_{x\%}$-COF**, starting with the calculation of their canonical 2D networks. Once different periodic models were constructed, they were fully optimized (simultaneous lattice/cell and structure optimizations) by DFT as implemented in the QUANTUM EXPRESSO plane-wave code [64]. For the periodic calculations, we adopted the GGA-PBE functional [65] to account for the XC effects, considering the efficient DFT-D3 semi-empirical vdW parametrization to add dispersion forces and energies to conventional DFT functionals [60]. To model the ion-electron interaction in the H, B, C, N and F atoms we have used ultra-soft pseudopotentials [64,66]. The Brillouin zones in all the periodic systems have been *k*-discretized by optimal (2 × 2 × 1) and (2 × 2 × 6) Monkhorst-Pack grids [67] for the 2D layers and 3D crystals, respectively. One-electron wave-functions were expanded in a basis of plane-waves with a kinetic energy cut-off of 46 and 380 Ry for the kinetic energy and electronic density, respectively, to achieve sufficient accuracy to guarantee a full convergence in total energy and electronic density. We carried out simultaneous full lattice/cell and structure optimizations for the different starting-point layered 3D system models within a conjugate gradient minimization scheme until the net force acting on any atom was below 0.02 $eVÅ^{-1}$. The crystal-bulk models have been analysed for several stacking-fashions, eclipsed (AA) and staggered (AB) configurations, and one intermediate at half-way between AA and AB, resulting the AA configuration the most stable one for both the **$BDP_{0\%}$-COF,** which is in excellent agreement with previous literature [17], and the **$BDP_{17\%}$-COF**, reinforcing its validity the excellent agreement between the experimental and simulated diffractograms.

3. Results and discussion

3.1. Synthesis and characterization of COFs

As mentioned above, including BODIPY derivatives in COFs can seriously affect pore size and crystallinity, crucial factors regarding its properties and possible applications, especially when a one-step synthetic methodology is required. This means a careful choice of the BODIPY to incorporate. Thus, knowing that the BODIPY core should be isostructural to **BPDA**, its design must comprise a similar size and two aldehyde groups, maintaining its fluorescent properties. This way, the 2,6-diformylBODIPYs stand out from the rest, having a simple synthesis and high fluorescence [68,69].

However, most of them have an aromatic substituent in their *meso* position, which is a potential drawback added to the known steric effects of the sp^3 centres, and, on the other hand, the only previously described diformylation in a *meso*-aliphatic BODIPY [70], leads to the insertion of a bulky enamine group and a drastic loss in fluorescence. Because of that, the best option is to use a BODIPY derivative without any substitution in its *meso*, 2 and 6 positions.

In this background, only one BODIPY has those features, the commercially available PM505/515 (**BDP**), and surprisingly, its diformylated derivative has not been previously described. Briefly, using the Vilsmeier-Haack reaction, the monoformylated **BDPMA** [57] is obtained with a 99% yield. Despite this, the synthesis of **BDPDA** is not trivial because, under standard reaction conditions (DCE), it decomposes. This has been solved by changing the solvent to DCM and using long reaction times, isolating **BDPDA** with 82% yield. Thus, a novel BODIPY derivative, showing the desired features for COFs synthesis, has been obtained following the two-step formylation sequence depicted in Scheme 3.

As shown in Scheme 2, **$BDP_{17\%}$-COF** was obtained by following the protocol previously reported for the synthesis of **ETTA-BPDA-COF** with slight modifications [19]. Thus, crystallization of **$BDP_{17\%}$-COF** was accomplished by the Schiff-base reaction between **ETTA**, **BPDA** and **BDPDA** catalysed with acetic acid (6 M) at 120 °C for 3 days by using solvothermal reaction conditions. For comparison purposes, the parent **ETTA-BPDA-COF**, named as **$BDP_{0\%}$-COF** in this study, was also synthesized.

The crystallinity of the obtained COFs was investigated by powder X-ray diffraction (PXRD). The experiments revealed that the modified **$BDP_{17\%}$-COF** displays a diffraction pattern similar to the one previously reported for **$BDP_{0\%}$-COF** (Figs. 1a, S1 and S2, respectively). This fact confirms that the introduction of the bulky BODIPY moiety does not significantly affect the Kagome lattice that remains practically unaltered due to the congruent nature of the **BPDA** and **BDPDA** segments. Thus, the **$BDP_{17\%}$-COF** exhibits diffraction maxima at 2.20°, 3.81°, 4.48°, 6.61°, 7.96° and 8.79°, which are consistent with those registered for **$BDP_{0\%}$-COF** at 2.20°, 3.94°, 4.44°, 6.67°, 7.95° and 8.84°. The synthesis

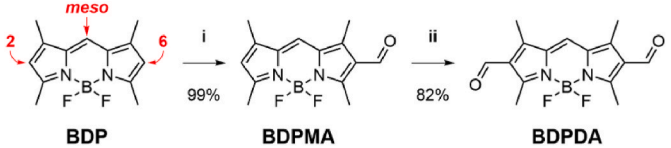

Scheme 3. Synthetic route towards **BDPDA** dopant. Reaction conditions: i. $POCl_3$, DMF, DCE, 60 °C, 1 h; ii. $POCl_3$, DMF, CH_2Cl_2, reflux, 48 h.

of **BDP$_{32\%}$-COF** and **BDP$_{100\%}$-COF** was also carried out. In these cases, mainly amorphous solids were obtained as shown in Fig. S3, highlighting the benefits of the strategy followed for the tuning of COFs' properties in the development of *ad-hoc* materials.

Density functional theory, as implemented in the localized basis set Gaussian16 [59] and the plane-wave QUANTUM ESPRESSO [64] atomistic simulation packages, has been used to solve the crystalline structure and compute the optical properties of the **BDP$_{17\%}$-COF** (further details in experimental section 2.4). Regarding the structure, after simultaneous lattice + cell geometrical optimizations, result of the calculations yield a purely hexagonal symmetry for this system with a lattice parameter of 47.12 Å (see Fig. 1b), in an eclipsed (AA) crystal stacking configuration with an interlayer distance of 4.49 Å, very close to the one theoretically obtained previously for **BDP$_{0\%}$-COF** [17]. This preferred stacking configuration has been predicted theoretically as the most energetically favourable one, among others checked, and its validity is reinforced by the excellent agreement between the simulated diffractogram on the basis of this structure and the experimental one (see Fig. 1a), not achieved for the other two stacking configurations tested (Fig. S4). Simulated diffractogram exhibits diffraction maxima at 2.13(2.20°), 3.90(3.81°), 4.44(4.48°), 6.67(6.61°), 7.95(7.96°) and 8.84 (8.79°) –experimental values in parentheses.

Likewise, the porous features were retained upon the doping. Nitrogen sorption isotherms at 77 K revealed a type I isotherm, characteristic of microporous materials, for both compounds (Fig. 1c). The Brunauer-Emmet-Teller (BET) surface area was calculated to be 287 m^2/g (Fig. S5) and 168 m^2/g (Fig. S6) for **BDP$_{17\%}$-COF** and **BDP$_{0\%}$-COF**, respectively. The pore volumes at 0.95 p/p° were estimated to be 0.231 cm^3/g for both materials. Finally, the pore sizes were calculated trough the non-local density functional theory (NLFDT) revealing wide distributions centred at 2.7 nm and 3.3 nm for **BDP$_{17\%}$-COF**, and 2.3 and 3.5 nm for **BDP$_{0\%}$-COF** (Figs. S7 and S8, respectively).

The successful polymerization to yield the COFs was monitored by ^{13}C cross-polarization magic-angle-spinning nuclear magnetic resonance (^{13}C-CP-MAS-NMR), revealing the fading of the aldehyde carbonylic functionalities around 190 ppm, the emergence of the imine linkages around 160 ppm for the **BP** and **BDP** moieties and the presence of the anisochronous aromatic carbons between 154 and 120 ppm. It is worth mentioning that the signals corresponding to the **BDP$_{17\%}$-COF** appear broadened, which is in accordance with the introduction of new anisochronous nuclei in comparison with the non-doped **BDP$_{0\%}$-COF**. Finally, in addition to the data mentioned above, the characteristic signals corresponding to the Csp^3 carbons of the BODIPY-methyl groups at 11 ppm confirms that the dopant was successfully introduced in the COF network (Fig. 1d). Furthermore, the polymerization was confirmed by Fourier transform infrared spectroscopy (FTIR), revealing the fading of the aldehyde (around 1680 cm^{-1} for both aldehydes) and amine (3444 and 3345 cm^{-1}) functionalities, as well as the emergence of the imine stretching band around 1622 cm^{-1} (Fig. S9).

Finally, the thermal stability of the doped product **BDP$_{17\%}$-COF** was investigated by means of thermogravimetric analysis (TGA), registering a minimum weight loss of less than 5% at temperatures below 400 °C without a prominent degradation of the network at 522 °C corresponding to the 33% of the initial mass (Fig. S10). These results are in concordance with that reported previously for the non-doped **BDP$_{0\%}$-COF** [19].

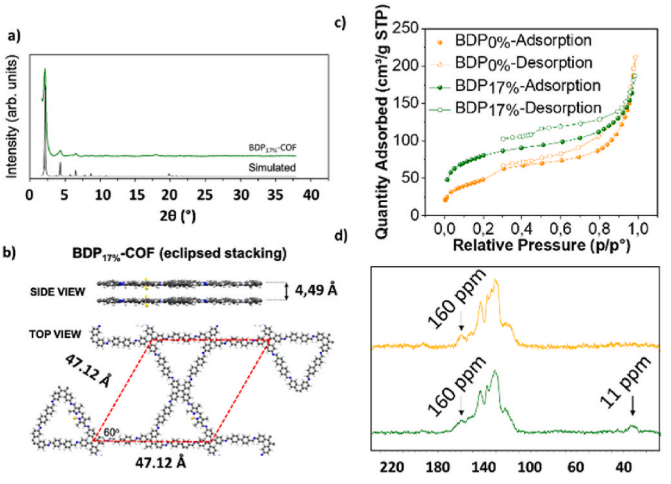

Fig. 1. a) Comparison between the experimental and the simulated PXRD of **BDP$_{17\%}$-COF**. **b)** Top and side pictorial views of the most stable computed structure for **BDP$_{17\%}$-COF**. **c)** N_2 sorption isotherms at 77K of **BDP$_{17\%}$-COF** (green) and **BDP$_{0\%}$-COF** (orange). **d)** ^{13}C-CP-MAS NMR spectra of **BDP$_{17\%}$-COF** (green line) and **BDP$_{0\%}$-COF** (orange line).

3.2. Production and characterization of CONs

To address the usually complex issue of the processing of COFs, we have investigated the bulk morphology of the **BDP$_{17\%}$-COF** by means of scanning electron microscopy (SEM). SEM micrographs revealed a polygranular composition for the **BDP$_{17\%}$-COF** (Fig. 2a and Figs. S11–S12) in good agreement with the morphology expected, which is favourable for the delamination of the COF grains in covalent organic nanosheets (CONs) *via* liquid phase exfoliation [55].

In this manner, COF powders were suspended in a (7/3) THF/water mixture in a 0.21 mg of COF/mL of mixture proportion. The system was acidulated with 1.1 μL of HCl (36%) per mL of mixture and the suspensions were subdued to an ultrasonic bath (35 kH, 80 W) for 1 h. The exfoliated materials were separated by centrifugation (6000 rpm, 45 min), collected with a glass pipette and filtered with a 0.22 μm nylon syringe filter. Finally, for the cell viability studies, the solvents were removed *in vacuo* and the solids were dried at 80 °C for 12 h. The colloidal nature of the obtained CONs was corroborated by Tyndall-effect upon irradiation with a laser beam. In addition, the colloids of **BDP$_{17\%}$-CONs**, as well as the non-doped **BDP$_{0\%}$-CONs**, were characterized by dynamic light scattering (DLS) revealing a monomodal distribution centred around 113 nm for both samples (Fig. 2b and S13-S14). Transmission electron microscopy (TEM) micrographs revealed the thin-layered structure of the exfoliated CONs (Fig. 2c and Figs. S15–S16). The FTIR spectra of the obtained material after the exfoliation conditions does not display the signals corresponding to the amine (3341 cm^{-1} for ETTA) or the aldehyde (1662 cm^{-1} for BDPDA and 1684 cm^{-1} for BPDA) functionalities. Furthermore, the FTIR spectra of the polymers after the exfoliation conditions match well with that found for the powder. Only the intensity of the imine stretching signal at 1622 cm^{-1} is slightly reduced. Furthermore, a new signal at 1651 cm^{-1} appeared which can be assigned to deformation $\delta(N^+\text{-}H)$ of the protonated imine bonds (Fig. S17).

Finally, UV-VIS and fluorescence spectroscopies of the as-obtained suspensions in THF/water mixtures revealed the introduction of the **BDP** units in the COF network by showing the new absorption (Fig. 3a) and emission (Fig. 3b) processes which match with the ones found for the **BDPDA** monomer.

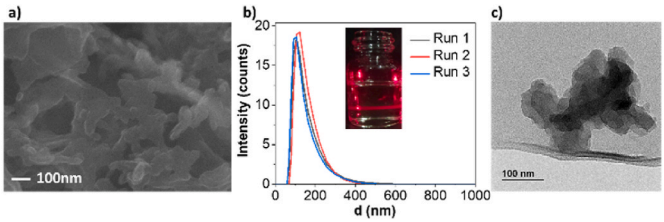

Fig. 2. a) SEM images of **BDP$_{17\%}$-COF** (scale bar 100 nm). **b)** DLS distribution of **BDP$_{17\%}$-CONs** in water (inset Tyndall effect). **c)** TEM image of **BDP$_{17\%}$-CONs** (scale bar 100 nm).

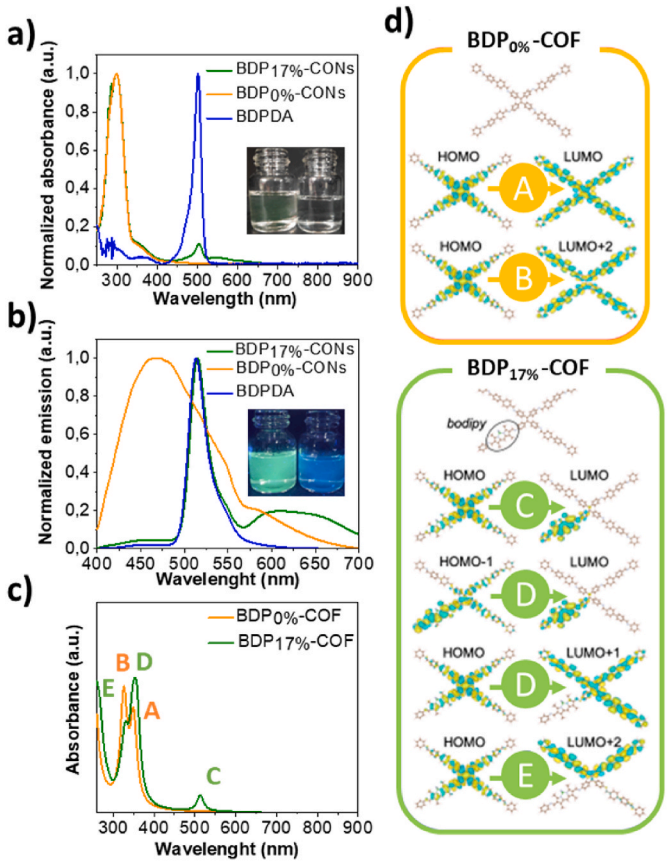

Fig. 3. a) Experimental UV–Vis absorption spectra of **$BDP_{17\%}$-COF**, **$BDP_{0\%}$-COF** and **BDPDA** colloids in THF/water (7/3, v/v). Inset: picture of the as obtained suspensions. **b)** Normalized emission spectra of **$BDP_{0\%}$-CONs** (orange) **$BDP_{17\%}$-CONs** (green) and **BDPDA** (black) in THF/H_2O (7/3). Inset: picture of the under irradiation with a 365 nm conventional lamp. **c)** TDDFT-computed UV–Vis absorption spectra of the molecular fragments representative of the **$BDP_{0\%}$-COF** and **$BDP_{17\%}$-COF** protonated in the imine central groups in THF/water (7/3). **d)** Optimized geometries of the representative **$BDP_{0\%}$-COF** and **$BDP_{17\%}$-COF** molecular fragments and related electronic transitions.

Fig. 3c shows the TDDFT-computed UV–Vis absorption spectra of molecular fragments representative of the **$BDP_{0\%}$-COF** and **$BDP_{17\%}$-COF** in a THF/water (7/3) mixture. There is an excellent agreement between the experimental (see Fig. 3a) and computed UV–Vis profiles, not only qualitatively, but also quantitatively, after consideration of the solvent effects within the calculations. It is worth mentioning at this point that this good agreement between experiment and theory is obtained by considering the protonation of the imine central groups. Optical properties have been also computed for the unprotonated systems yielding significantly different photo-absorption spectra, impossible to compare with the experimental ones, which reinforces the scenario of the protonated imine central groups. The protonation rigidizes the bond and hinders the dissipation of absorbed energy across the structure, which enables absorption and emission signatures within the visible range [12].

The theoretical spectra exhibited by the molecular building blocks show a wide absorption region common to both structures which is located between 300 and 375 nm and which is composed of two main absorptions with maxima at 315–325 and 365–375 nm, respectively. This broad adsorption region is also observed in the experimental spectra for both systems centred around 300 nm. Nonetheless, for the **$BDP_{17\%}$-COF** fragment we can observe in the theoretical spectrum a peak at 515 nm, which is not visible for the **$BDP_{0\%}$-COF** fragment. This absorption can be clearly associated with the presence of the BODIPY building block and perfectly matches that observed in the experimental spectrum at *ca* 500 nm, which can be detected only for the **$BDP_{17\%}$-COF**. The origin of all these absorptions can be understood from the depiction of the 3D topology of the initial and final orbital states involved in the main electronic transitions (Fig. 3d). Absorption maxima A and B for the **$BDP_{0\%}$-COF** (Fig. 3c) correspond respectively to HOMO → LUMO and HOMO → LUMO+2 transitions (Fig. 3d). Nonetheless, the presence of the BODIPY building block in **$BDP_{17\%}$-COF** reduces dramatically the orbital symmetry in comparison with **$BDP_{0\%}$-COF** and the absorptions observed for **$BDP_{17\%}$-COF** (C, D and E, Fig. 3c) correspond to four transitions which are HOMO → LUMO (absorption maximum C), HOMO-1 → LUMO and HOMO → LUMO+1 (both contributing to absorption maximum D) and HOMO LUMO +2 (absorption maximum E). Especially remarkable is the presence of the absorption maximum C of the **$BDP_{17\%}$-COF** fragment. This absorption is exclusive for the **$BDP_{17\%}$-COF** fragment and corresponds to the lowest electronic transition of the system from the HOMO to the LUMO, located exclusively in the BODIPY within the structure, which justifies its observation just for the **$BDP_{17\%}$-COF**. This absorption peak within the visible region is responsible for the different emission colour observed after the photoexcitation for **$BDP_{17\%}$-COF** and **$BDP_{0\%}$-COF**. While **$BDP_{0\%}$-COF** exhibits a moderate blue coloured fluorescence, the **$BDP_{17\%}$-COF** shows a stronger green fluorescence (Fig. 3b).

3.3. Cell viability of CONs

The strict control on the nanolayer dimensions and the fluorescence exhibited by the **$BDP_{17\%}$-CONs** make of it a good candidate to be explored for biomedical applications and in particular in photodynamic therapy (PDT) for cancer treatment. Photodynamic therapy is a promising non-invasive method based on the use of light-absorbing agents such as a BODIPY, to trigger a toxic effect by generating reactive oxygen species (ROS) after its irradiation in the presence of oxygen to kill cancer cells. The development of new nanomaterials is gaining attention for improving PDT and agents [31–33].

Here, as a proof of concept, we have evaluated the biological behaviour of **$BDP_{17\%}$-CONs** in tumoral cells. In a first step, the possible toxicity of the material was studied in human melanoma Sk-Mel-103 cells. For that purpose, the Sk-Mel-103 cells were treated with different concentrations of both non-doped **$BDP_{0\%}$-CONs** and doped **$BDP_{17\%}$-CONs** for 48 h, and cell viability was measured by using cell proliferation WST-1 reagent. The results demonstrated that both COF materials were well-tolerated by the cells, showing ca. 100% cell viability at concentrations as high as 250 μg/mL, thus discarding any possible cytotoxic effect (Fig. 4).

Finally, due to the fluorescent characteristics of **$BDP_{17\%}$-CONs**, we evaluated the potential ability of the nanoparticles to be endocytosed by cancer cells by confocal microscopy assays. Endocytosis is a well-established mechanism of nanomaterials uptake, being the structure, size, and porosity of the material key factors that could affect internalization and therefore their suitability for biomedical applications [71–73]. In this case, we monitored the uptake of **$BDP_{17\%}$-CONs** in the

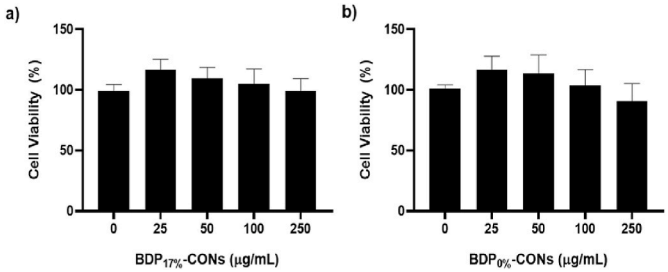

Fig. 4. Cell viability assays in Sk-Mel-103 with **a) $BDP_{0\%}$-CONs** and **b) $BDP_{17\%}$-CONs**. Data represent the mean ± SEM (standard error of the mean) of at least three independent experiments.

presence of a cell membrane marker. As can be observed (Fig. S18), the **BDP$_{17\%}$-CONs** material is effectively internalized by Sk-Mel-103 cells and high magnified images showed the clear green signal inside the cells, associated with BODIPY fluorescence, after 24 h of incubation with the **BDP$_{17\%}$-CONs**, which is retained for at least two more days (Fig. 5). All these results suggest the proper internalization of the prepared **BDP$_{17\%}$-CONs** in cancer cells.

4. Conclusions

The work presented here shows a new strategy to develop efficient BODIPY@COF-based bioimaging materials by a pre-synthetic doping of COFs whose density can be systematically designed and synthetically controlled. The doped network can be obtained without compromising the structural and porous features of the parent crystalline framework as corroborated by PXRD and N_2 sorption isotherms. The materials were processed into colloidal CONs, which were characterized by UV-VIS and emission spectroscopies, revealing the incorporation of the BODIPY dye. These nanomaterials showed a particle size around 100 nm, suitable for cell internalization as imaging studies demonstrated. Remarkably the developed material did not exhibit any sign of toxicity in cells. This kind of modifications allows to improve the use of COF material and expand its future applications. In light of the results obtained in this research, we anticipate that **BDP$_{17\%}$-COF** and the corresponding colloidal **BDP$_{17\%}$-CONs** through this synthetic strategy may hold great potential to develop advanced organic frameworks directed to new biomedical applications such as photodynamic therapy and/or phototheragnosis. Further work in this area is in progress in our laboratories to optimize the material design and attachment of BODIPY moieties.

CRediT authorship contribution statement

Fátima Suárez-Blas: Investigation, Data curation, Visualization, Writing – original draft, Writing – review & editing. **Marcos Martínez-**

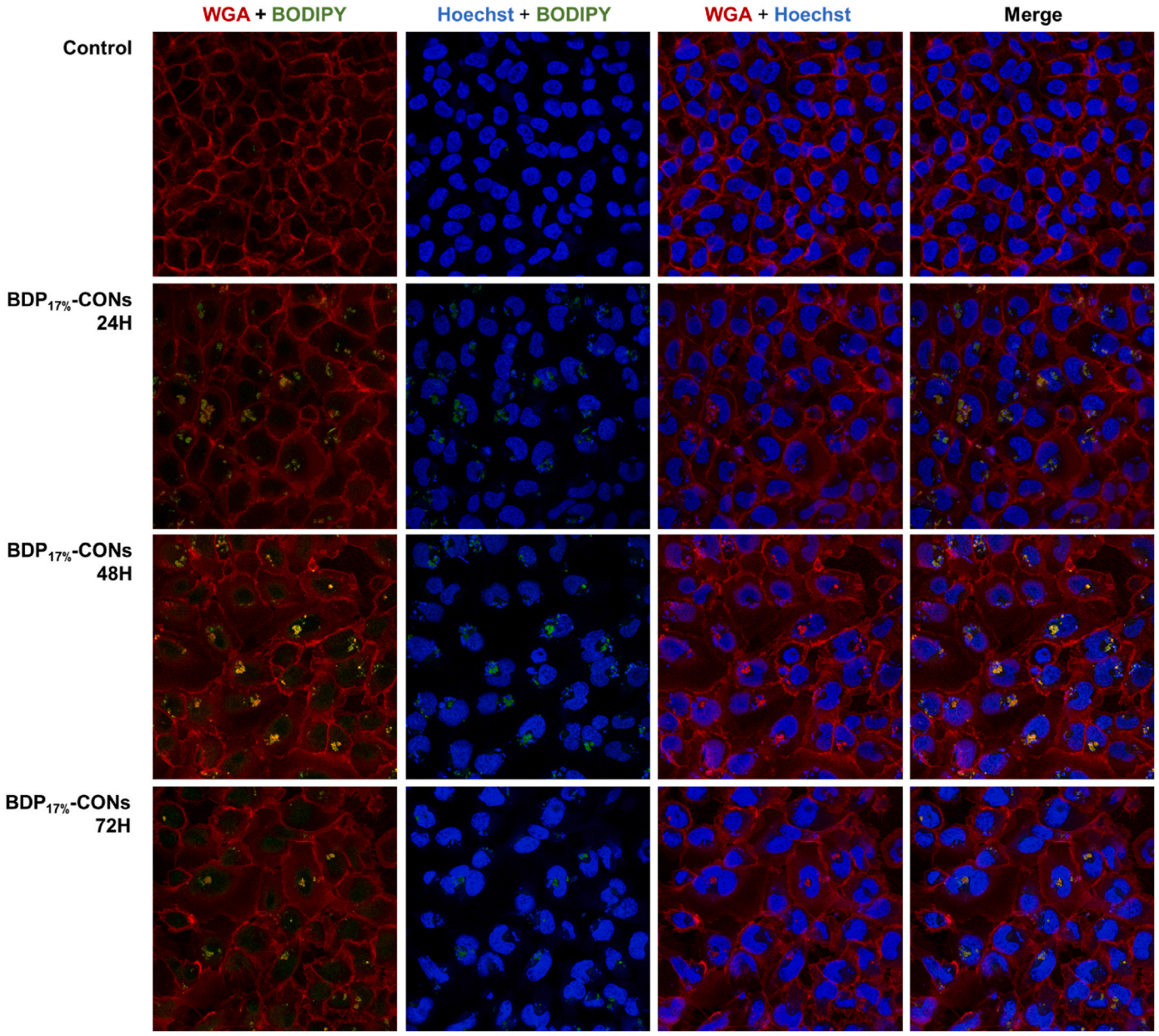

Fig. 5. Confocal images at higher magnification of BDP$_{17\%}$-CONs uptake in Sk-Mel-103 cells after 24,28 and 72 h. BODIPY-associated fluorescence (green), DNA marker Hoechst 33342 (blue), and cell membrane marker WGA (red). Representative images of the confocal experiments in at least three independent experiments.

Fernández: Investigation, Data curation, Visualization, Writing – original draft, Writing – review & editing. **Alejandro Prieto-Castañeda:** Investigation, Data curation, Visualization, Writing – original draft, Writing – review & editing. **Alba García-Fernández:** Investigation, Data curation, Visualization, Writing – original draft, Writing – review & editing. **José I. Martínez:** Investigation, Data curation, Visualization, Writing – original draft, Writing – review & editing. **María Mar Ramos:** Investigation, Data curation, Visualization, Writing – original draft, Writing – review & editing. **María J. Ortiz:** Conceptualization, Investigation, Data curation, Visualization, Writing – original draft, Writing – review & editing, Funding acquisition. **Ramón Martínez-Máñez:** Conceptualization, Investigation, Data curation, Visualization, Writing – original draft, Writing – review & editing, Funding acquisition. **José L. Segura:** Conceptualization, Investigation, Visualization, Supervision, Writing – review & editing, Funding acquisition, Project administration.

Declaration of competing interest

The authors declare that they have no known competing financial interests or personal relationships that could have appeared to influence the work reported in this paper

Data availability

Data will be made available on request.

Acknowledgements

This work was financially supported by Spanish MICINN (PID2019-106268GB-C33, TED2021-129886B-C43, PID2020-114755GB-C32, PID2020-113142RB-C21 and PLEC2021-007906), as well as by project PID2021-126304OB-C41 *via* MCIN/AEI/10.13039/501100011033/, by European Regional Development Fund - A way of doing Europe and by the Generalitat Valenciana (CIPROM/2021/007). J.I.M. also acknowledges funding from EU *via* the European Graphene Flagship (Grant Graphene Core3 881603) and Comunidad de Madrid (Grants S2018/NMT-4367 and Y2020/NMT-6469).

Appendix A. Supplementary data

Supplementary material (materials and general methods; details of the synthesis, characterization and methods of the polymeric materials; details of the theoretical methods; supporting figures including PXRD, FTIR spectrum, nitrogen isotherm profile, pore size distribution profile, TGA curve, TEM and SEM images of the COFs; confocal images; and supporting references) can be found online at https://doi.org/10.1016/j.dyepig.2023.111561.

References

[1] Diercks CS, Yaghi OM. The atom, the molecule, and the covalent organic framework. Science 2017;355(6328):eaal1585. https://doi.org/10.1126/science.aal1585.
[2] Hu J, Gupta SK, Ozdemir J, Beyzavi H. Applications of dynamic covalent Chemistry concept toward tailored covalent organic framework nanomaterials: a review. ACS Appl Nano Mater 2020;3(7):6239–69. https://doi.org/10.1021/acsanm.0c01327.
[3] Del Giudice D, Valentini M, Melchiorre G, Spatola E, Di Stefano S. Dissipative dynamic covalent Chemistry (DDCvC) based on the transimination reaction. Chem Eur J 2022;28(26):e202200685. https://doi.org/10.1002/chem.202200685.
[4] Kandambeth S, Dey K, Banerjee R. Covalent organic frameworks: Chemistry beyond the structure. J Am Chem Soc 2019;141(5):1807–22. https://doi.org/10.1021/jacs.8b10334.
[5] Martínez-Fernández M, Martínez-Periñán E, Royuela S, Martínez JI, Zamora F, Lorenzo E, et al. Covalent organic frameworks based on electroactive naphthalenediimide as active electrocatalysts toward oxygen reduction reaction. Appl Mater Today 2022;26:101384. https://doi.org/10.1016/j.apmt.2022.101384.
[6] Kim HM, Jang HK, Hwang TG, Namgoong JW, Kim JY, Yuk SB, et al. Comparative study of the synthetic methods for perylene-based covalent triazine polyimides. Dyes Pigments 2021;186:108968. https://doi.org/10.1016/j.dyepig.2020.108968.
[7] Zhang K, Niu C, Yu C, Zhang L, Xu Y. Highly crystalline vinylene-linked covalent organic frameworks enhanced solid polycarbonate electrolyte for dendrite-free solid lithium metal batteries. Nano Res 2022;15(9):8083–90. https://doi.org/10.1007/s12274-022-4480-6.
[8] Geng K, He T, Liu R, Dalapati S, Tan KT, Li Z, et al. Covalent organic frameworks: design, synthesis, and functions. Chem Rev 2020;120(16):8814–933. https://doi.org/10.1021/acs.chemrev.9b00550.
[9] Yao R, Deng B, Li Z, Xie L, Li J, Tuo K, et al. A covalent organic framework rich in lanthanide Eu3+ binding sites for sensitive and selective determination of tetracycline. Dyes Pigments 2023;213:111159. https://doi.org/10.1016/j.dyepig.2023.111159.
[10] Zhao X, Pachfule P, Thomas A. Covalent organic frameworks (COFs) for electrochemical applications. Chem Soc Rev 2021;50(12):6871–913. https://doi.org/10.1039/D0CS01569E.
[11] Segura JL, Royuela S, Mar Ramos M. Post-synthetic modification of covalent organic frameworks. Chem Soc Rev 2019;48(14):3903–45. https://doi.org/10.1039/C8CS00978C.
[12] Martínez-Fernández M, Gavara R, Royuela S, Fernández-Ecija L, Martínez JI, Zamora F, et al. Following the light: 3D-printed COF@poly(2-hydroxyethyl methacrylate) dual emissive composite with response to polarity and acidity. J Mater Chem 2022;10(9):4634–43. https://doi.org/10.1039/D1TA09614A.
[13] Xu H, Gao J, Jiang D. Stable, crystalline, porous, covalent organic frameworks as a platform for chiral organocatalysts. Nat Chem 2015;7(11):905–12. https://doi.org/10.1038/nchem.2352.
[14] Ren X-R, Bai B, Zhang Q, Hao Q, Guo Y, Wan L-J, et al. Constructing stable chromenoquinoline-based covalent organic frameworks via intramolecular Povarov reaction. J Am Chem Soc 2022;144(6):2488–94. https://doi.org/10.1021/jacs.1c13005.
[15] Grunenberg L, Savasci G, Terban MW, Duppel V, Moudrakovski I, Etter M, et al. Amine-Linked covalent organic frameworks as a platform for postsynthetic structure interconversion and pore-wall modification. J Am Chem Soc 2021;143(9):3430–8. https://doi.org/10.1021/jacs.0c12249.
[16] Yang F, Qu J, Zheng Y, Cai Y, Yang X, Li CM, et al. Recent advances in high-crystalline conjugated organic polymeric materials for photocatalytic CO2 conversion. Nanoscale 2022;14(41):15217–41. https://doi.org/10.1039/D2NR04727F.
[17] Vardhan H, Al-Enizi AM, Nafady A, Pan Y, Yang Z, Gutiérrez HR, et al. Single-pore versus dual-pore bipyridine-based covalent–organic frameworks: an insight into the heterogeneous catalytic activity for selective C H functionalization. Small 2021;17(22):2003970. https://doi.org/10.1002/smll.202003970.
[18] Bunck DN, Dichtel WR. Mixed linker strategies for organic framework functionalization. Chem Eur J 2013;19(3):818–27. https://doi.org/10.1002/chem.201203145.
[19] Pang Z-F, Xu S-Q, Zhou T-Y, Liang R-R, Zhan T-G, Zhao X. Construction of covalent organic frameworks bearing three different kinds of pores through the heterostructural mixed linker strategy. J Am Chem Soc 2016;138(14):4710–3. https://doi.org/10.1021/jacs.6b01244.
[20] Treibs A, Kreuzer F-H. Difluorboryl-Komplexe von Di- und Tripyrrylmethenen. Justus Liebigs Ann Chem 1968;718(1):208–23. https://doi.org/10.1002/jlac.19687180119.
[21] Yuan L, Su Y, Cong H, Yu B, Shen Y. Application of multifunctional small molecule fluorescent probe BODIPY in life science. Dyes Pigments 2022;208:110851. https://doi.org/10.1016/j.dyepig.2022.110851.
[22] Shah M, Thangaraj K, Soong M-L, Wolford LT, Boyer JH, Politzer IR, et al. Pyrromethene–BF2 complexes as laser dyes:1. Heteroat Chem 1990;1(5):389–99. https://doi.org/10.1002/hc.520010507.
[23] Boyer JH, Haag AM, Sathyamoorthi G, Soong M-L, Thangaraj K, Pavlopoulos TG. Pyrromethene–BF2 complexes as laser dyes: 2. Heteroat Chem 1993;4(1):39–49. https://doi.org/10.1002/hc.520040107.
[24] Boens N, Verbelen B, Ortiz MJ, Jiao L, Dehaen W. Synthesis of BODIPY dyes through postfunctionalization of the boron dipyrromethene core. Coord Chem Rev 2019;399:213024. https://doi.org/10.1016/j.ccr.2019.213024.
[25] Bumagina NA, Antina EV, Ksenofontov AA, Antina LA, Kalyagin AA, Berezin MB. Basic structural modifications for improving the practical properties of BODIPY. Coord Chem Rev 2022;469:214684. https://doi.org/10.1016/j.ccr.2022.214684.
[26] Poddar M, Misra R. Recent advances of BODIPY based derivatives for optoelectronic applications. Coord Chem Rev 2020;421:213462. https://doi.org/10.1016/j.ccr.2020.213462.
[27] Squeo BM, Ganzer L, Virgili T, Pasini M. BODIPY-based molecules, a platform for photonic and solar cells. Molecules 2020;26(1). https://doi.org/10.3390/molecules26010153.
[28] Bañuelos J. BODIPY dye, the most versatile fluorophore ever? Chem Rec 2016;16(1):335–48. https://doi.org/10.1002/tcr.201500238.
[29] Boens N, Leen V, Dehaen W. Fluorescent indicators based on BODIPY. Chem Soc Rev 2012;41(3):1130–72. https://doi.org/10.1039/C1CS15132K.
[30] Mao Z, Kim JH, Lee J, Xiong H, Zhang F, Kim JS. Engineering of BODIPY-based theranostics for cancer therapy. Coord Chem Rev 2023;476:214908. https://doi.org/10.1016/j.ccr.2022.214908.
[31] Van Straten D, Mashayekhi V, De Bruijn HS, Oliveira S, Robinson DJ. Oncologic photodynamic therapy: basic principles, current clinical status and future directions. Cancers 2017;9(2):19.
[32] Nanoparticles for Advanced Photodynamic Therapy of Cancer. Photomedicine and Laser Surgery 2017;35(11):581–8. https://doi.org/10.1089/pho.2017.4308.
[33] Zhao X, Liu J, Fan J, Chao H, Peng X. Recent progress in photosensitizers for overcoming the challenges of photodynamic therapy: from molecular design to

application. Chem Soc Rev 2021;50(6):4185–219. https://doi.org/10.1039/D0CS00173B.
[34] Zhang W, Ahmed A, Cong H, Wang S, Shen Y, Yu B. Application of multifunctional BODIPY in photodynamic therapy. Dyes Pigments 2021;185:108937. https://doi.org/10.1016/j.dyepig.2020.108937.
[35] Kolemen S, Akkaya EU. Reaction-based BODIPY probes for selective bio-imaging. Coord Chem Rev 2018;354:121–34. https://doi.org/10.1016/j.ccr.2017.06.021.
[36] Marfin YS, Solomonov AV, Timin AS, Rumyantsev EV. Recent advances of individual BODIPY and BODIPY-based functional materials in medical diagnostics and treatment. Curr Med Chem 2017;24(25):2745–72. https://doi.org/10.2174/0929867324666170601092327.
[37] Chen D, Zhong Z, Ma Q, Shao J, Huang W, Dong X. Aza-BODIPY-based nanomedicines in cancer phototheranostics. ACS Appl Mater Interfaces 2020;12(24):26914–25. https://doi.org/10.1021/acsami.0c05021.
[38] Cheng H-B, Cao X, Zhang S, Zhang K, Cheng Y, Wang J, et al. BODIPY as multifunctional theranostic reagent in biomedicine: self-assembly, properties and applications. Adv Mater 2023;35:2207546. https://doi.org/10.1002/adma.202207546.
[39] Gupta G, Sun Y, Das A, Stang PJ, Yeon Lee C. BODIPY based metal-organic macrocycles and frameworks: recent therapeutic developments. Coord Chem Rev 2022;452:214308. https://doi.org/10.1016/j.ccr.2021.214308.
[40] Lei Z, Zhang F. Molecular engineering of NIR-II fluorophores for improved biomedical detection. Angew Chem Int Ed 2021;60(30):16294–308. https://doi.org/10.1002/anie.202007040.
[41] Dai H, Shen Q, Shao J, Wang W, Gao F, Dong X. Small molecular NIR-II fluorophores for cancer phototheranostics. Innovation (Camb) 2021;2(1):100082. https://doi.org/10.1016/j.xinn.2021.100082.
[42] Liu X, Yu B, Shen Y, Cong H. Design of NIR-II high performance organic small molecule fluorescent probes and summary of their biomedical applications. Coord Chem Rev 2022;468:214609. https://doi.org/10.1016/j.ccr.2022.214609.
[43] Feng L, Qian C, Zhao Y. Recent advances in covalent organic framework-based nanosystems for bioimaging and therapeutic applications. ACS Mater Lett 2020;2(9):1074–92. https://doi.org/10.1021/acsmaterialslett.0c00260.
[44] Kim JH, Kang DW, Yun H, Kang M, Singh N, Kim JS, et al. Post-synthetic modifications in porous organic polymers for biomedical and related applications. Chem Soc Rev 2022;51(1):43–56. https://doi.org/10.1039/D1CS00804H.
[45] Yazdani H, Shahbazi M-A, Varma RS. 2D and 3D covalent organic frameworks: cutting-edge applications in biomedical sciences. ACS Appl Bio Mater 2022;5(1):40–58. https://doi.org/10.1021/acsabm.1c01015.
[46] Li S, Zhao B, Kan W, Song T, Zheng W, Qi X, et al. A fluorescent covalent organic framework with a brick-wall topology for the detection of Cu2+ promoted by the associated mechanism. Dyes Pigments 2023;214:111178. https://doi.org/10.1016/j.dyepig.2023.111178.
[47] Gong W, Dong Y, Liu C, Shi H, Yin M, Li W, et al. Hydrazone-linked luminescent covalent organic frameworks based on AIE-active unit for acid vapour sensing. Dyes Pigments 2022;204:110464. https://doi.org/10.1016/j.dyepig.2022.110464.
[48] Yang L, Lu H, Zhang T, Zhou S, Yang X, Luo Z, et al. Novel water-dispersible lanthanide-grafted covalent organic framework nanoplates for luminescent levofloxacin sensing and visual pH detection. Dyes Pigments 2021;196:109818. https://doi.org/10.1016/j.dyepig.2021.109818.
[49] Zhou S, Meng T, Hu D, Zhu Y, Huang C, Song M, et al. Characteristic synthesis of a covalent organic framework and its application in multifunctional tumor therapy. ACS Appl Bio Mater 2022;5(1):59–81. https://doi.org/10.1021/acsabm.1c01039.
[50] Valenzuela C, Chen C, Sun M, Ye Z, Zhang J. Strategies and applications of covalent organic frameworks as promising nanoplatforms in cancer therapy. J Mater Chem B 2021;9(16):3450–83. https://doi.org/10.1039/D1TB00041A.
[51] Guan Q, Fu D-D, Li Y-A, Kong X-M, Wei Z-Y, Li W-Y, et al. BODIPY-decorated nanoscale covalent organic frameworks for photodynamic therapy. iScience 2019;14:180–98. https://doi.org/10.1016/j.isci.2019.03.028.
[52] Guan Q, Zhou L-L, Lv F-H, Li W-Y, Li Y-A, Dong Y-B. A glycosylated covalent organic framework equipped with BODIPY and CaCO3 for synergistic tumor therapy. Angew Chem Int Ed 2020;59(41):18042–7. https://doi.org/10.1002/anie.202008055.
[53] Dong X-J, Li W-Y, Guan Q, Li Y-A, Dong Y-B. A CuS- and BODIPY-loaded nanoscale covalent organic framework for synergetic photodynamic and photothermal therapy. Chem Commun 2022;58(14):2387–90. https://doi.org/10.1039/D1CC06330H.
[54] Xing G, Zheng W, Gao L, Zhang T, Wu X, Fu S, et al. Nonplanar rhombus and Kagome 2D covalent organic frameworks from distorted aromatics for electrical conduction. J Am Chem Soc 2022. https://doi.org/10.1021/jacs.1c13534.
[55] Fan Y, Zhang J, Shen Y, Zheng B, Zhang W, Huo F. Emerging porous nanosheets: from fundamental synthesis to promising applications. Nano Res 2021;14(1):1–28. https://doi.org/10.1007/s12274-020-3082-4.
[56] Peng Y, Huang M, Chen L, Gong C, Li N, Huang Y, et al. Ultrathin covalent organic framework nanosheet-based photoregulated metal-free oxidase-like nanozyme. Nano Res 2022;15(10):8783–90. https://doi.org/10.1007/s12274-022-4541-x.
[57] Paulson CN, Guan X, Ayoub AM, Chan A, Karim RM, Pomerantz WCK, et al. Design, synthesis, and characterization of a fluorescence polarization Pan-BET bromodomain probe. ACS Med Chem Lett 2018;9(12):1223–9. https://doi.org/10.1021/acsmedchemlett.8b00380.
[58] Cakmak Y, Kolemen S, Duman S, Dede Y, Dolen Y, Kilic B, et al. Designing excited states: theory-guided access to efficient photosensitizers for photodynamic action. Angew Chem Int Ed 2011;50(50):11937–41. https://doi.org/10.1002/anie.201105736.
[59] Frisch MJ, Trucks GW, Schlegel HB, Scuseria GE, Robb MA, Cheeseman JR, et al. Gaussian 16 Rev. C.01. 2016. Wallingford, CT.
[60] Grimme S. Semiempirical GGA-type density functional constructed with a long-range dispersion correction. J Comput Chem 2006;27(15):1787–99. https://doi.org/10.1002/jcc.20495.
[61] Yanai T, Tew DP, Handy NC. A new hybrid exchange–correlation functional using the Coulomb-attenuating method (CAM-B3LYP). Chem Phys Lett 2004;393(1):51–7. https://doi.org/10.1016/j.cplett.2004.06.011.
[62] Casida ME. Time-dependent density functional response theory for molecules. Recent Advances in Density Functional Methods. WORLD SCIENTIFIC; 1995. p. 155–92.
[63] Tomasi J, Mennucci B, Cammi R. Quantum mechanical Continuum solvation models. Chem Rev 2005;105(8):2999–3094. https://doi.org/10.1021/cr9904009.
[64] Giannozzi P, Baroni S, Bonini N, Calandra M, Car R, Cavazzoni C, et al. QUANTUM ESPRESSO: a modular and open-source software project for quantum simulations of materials. J Phys Condens Matter 2009;21(39):395502. https://doi.org/10.1088/0953-8984/21/39/395502.
[65] Perdew JP, Burke K, Ernzerhof M. Generalized gradient approximation made simple. Phys Rev Lett 1996;77(18):3865–8. https://doi.org/10.1103/PhysRevLett.77.3865.
[66] Rappe AM, Rabe KM, Kaxiras E, Joannopoulos JD. Optimized pseudopotentials. Phys Rev B 1990;41(2):1227–30. https://doi.org/10.1103/PhysRevB.41.1227.
[67] Pack JD, Monkhorst HJ. "Special points for Brillouin-zone integrations"—a reply. Phys Rev B 1977;16(4):1748–9. https://doi.org/10.1103/PhysRevB.16.1748.
[68] Jiao L, Yu C, Li J, Wang Z, Wu M, Hao E. β-Formyl-BODIPYs from the Vilsmeier−Haack reaction. J Org Chem 2009;74(19):7525–8. https://doi.org/10.1021/jo901407h.
[69] Yu C, Jiao L, Yin H, Zhou J, Pang W, Wu Y, et al. α-/β-Formylated boron–dipyrrin (BODIPY) dyes: regioselective syntheses and photophysical properties. Eur J Org Chem 2011;2011(28):5460–8. https://doi.org/10.1002/ejoc.201100736.
[70] Palao-Utiel E, Montalvillo-Jiménez L, Esnal I, Prieto-Montero R, Agarrabeitia AR, García-Moreno I, et al. Controlling Vilsmeier-Haack processes in meso-methylBODIPYs: a new way to modulate finely photophysical properties in boron dipyrromethenes. Dyes Pigments 2017;141:286–98. https://doi.org/10.1016/j.dyepig.2017.02.030.
[71] Nel A, Xia T, Mädler L, Li N. Toxic potential of materials at the nanolevel. Science 2006;311(5761):622–7. https://doi.org/10.1126/science.1114397.
[72] Gratton SEA, Ropp PA, Pohlhaus PD, Luft JC, Madden VJ, Napier ME, et al. The effect of particle design on cellular internalization pathways. Proc Natl Acad Sci USA 2008;105(33):11613–8. https://doi.org/10.1073/pnas.0801763105.
[73] Verma A, Stellacci F. Effect of surface properties on nanoparticle–cell interactions. Small 2010;6(1):12–21. https://doi.org/10.1002/smll.200901158.